Third AO4ELT Conference - Adaptive Optics for Extremely Large Telescopes
Florence, Italy. May 2013
ISBN: 978-88-908876-0-4
DOI: 10.12839/AO4ELT3.13487

Wind profiling via slope detection and ranging: algorithm formulation and performance analysis for laser guide star tomography on extremely large telescopes

Luc Gilles[1] and Brent Ellerbroek[1]

[1]Thirty Meter Telescope Observatory Corporation, 1200 E. California Blvd, MC 102-8, Pasadena, CA 91125, USA

Abstract. This paper discusses a wind profile estimation algorithm for laser guide star tomography adaptive optics systems, which generalizes a previously published slope detection and ranging turbulence profiler [Gilles and Ellerbroek, J. Opt. Soc. Am. A**27**, A76 (2010)] to the case of spatio-temporal cross-correlations between a single or multiple pairs of wavefront sensors. The estimated wind profile is fed to a computationally efficient Distributed Kalman Filter to perform atmospheric tomography. Residual wavefront error is assessed for the Thirty Meter Telescope and compared to that of a static, single-frame, minimum mean square error estimator. We found that the superior turbulence rejection of the Kalman filter is a delicate feature requiring wind profile estimation to better than ~20% accuracy.

1. Introduction

Tomographic wavefront reconstruction using laser guide stars (LGSs) is under development for adaptive optics (AO) systems on extremely large telescopes (ELTs) [1-4], and a large amount of work has been performed in the last few years to develop computationally efficient algorithms and techniques to solve the challenging tomography step [5-9]. It has recently been shown that a non-negligible improvement in residual wavefront error (WFE) can be achieved with a predictive distributed Kalman filter (DKF), under the assumption of frozen flow and accurate knowledge of the turbulence and wind profiles [10]. Poyneer has studied in detail the validity of the frozen flow hypothesis, and found that the atmosphere is stable enough over 10s intervals for predictive Kalman filter algorithms to measure and adapt to the prevailing atmospheric conditions [11]. Along those lines, she has developed a computationally efficient Fourier-based predictive Kalman filter that is implemented on the Gemini Planet Imager (GPI) high-contrast AO system [12,13]. Her algorithm identifies layers of frozen flow, but does not provide information on the altitude of those layers. Such information is important for tomographic controllers, and Wang has shown that it can be retrieved from slope detection and ranging (SLODAR), i.e. spatio-temporal cross-correlations between the measurements of different wavefront sensors (WFSs) [14]. His algorithm tracks correlation peaks and has been implemented on the Gemini multi conjugate adaptive optics (MCAO) system (GeMS) [15].

The algorithm discussed in this paper is based on earlier work by the authors on turbulence (Cn2) profiling via SLODAR [16], but instead of tracking correlation peaks, the algorithm relies on a linear model relating the SLODAR data to the product of the wind and Cn2 profiles, therefore requiring two separate estimation steps.

Two important Monte Carlo simulation results are presented in this paper for the Thirty Meter Telescope (TMT) LGS MCAO system: (i) in the limit of perfect Cn2 and wind profile information, DKF provides ~35nm lower residual wavefront error (WFE) than a static minimum mean square error (MMSE) estimator augmented with a perfect predictor (a result that holds both at finite and infinite signal-to-noise ratio (SNR), illustrating the improved turbulence rejection properties of Kalman filtering as reported in [17]), and (ii) coupled with the Cn2 and wind profiling algorithm discussed in this paper, the performance gain drops to just a few nm, illustrating that accurate (better than ~20% error level) wind profile information is required for tomographic Kalman filters to retain their performance advantage. The paper is organized as follows. Section 2 provides a top-level description of the Cn2 and wind profile estimation algorithm, and simulation results are presented in Section 3.

2. Cn2 and wind profile estimation algorithm top-level description

We start with the mathematical expression of SLODAR data:

$$b_j^{\alpha}(\tau) = \left\langle m_{\alpha}(x_p, t) m_{\alpha}^{'}(x_p + d_j, t+\tau) \right\rangle_{x_p, t} \tag{2.1}$$

where x_p denotes the 2D pupil plane coordinate, $\alpha = x, y$ denotes measurement direction, j is the baseline number, d_j the baseline vector, m and m' the pair of measurements, and τ time delay. Note that baseline vectors d_j in (2.1) should be chosen to span a 2D vector space in order to provide 360deg velocity direction sensitivity. Baselines aligned along a line are insensitive to a velocity vector orthogonal to that line. A Fourier expression for $m_{\alpha}(x_p, t=0)$ was developed in [16]. Assuming frozen flow, i.e. phase at layer k evolving according to $\phi_k(x', y', t) = \phi_k(x' + \mathrm{v}_k t, y' + \mathrm{v}_k t, t=0)$ allows us to express (2.1) as follows:

$$b_j^{\alpha}(\tau) = \sum_{k=1}^{n_l} A_{jk}^{\alpha}(\tau, \mathrm{v}_k) p_k \tag{2.2}$$

where $p_k = r_{0,k}^{-5/3}$ (strength of turbulence layer k), and $A_{jk}^{\alpha}(\tau, \mathrm{v}_k)$ is a nonlinear function of v_k given by Eq.(24) in [16] with the following substitution:

$$\mathrm{PSD}_0(f_k^{'}) \rightarrow \mathrm{PSD}_0(f_k^{'}, \tau) = \mathrm{PSD}_0(f_k^{'}) \exp(2i\pi f_k^{'T} \mathrm{v}_k \tau) \tag{2.3}$$

where $f_k^{'}$ denotes the 2D spatial frequency vector for layer k in a cone coordinate system, and PSD_0 is a unit strength von Kármán power spectral density (PSD). The complex exponential can be expanded in Taylor series to yield:

$$b(\tau) = A(\mathrm{v}, \tau) p = b(\tau = 0) + \tau C q + \mathcal{O}(\tau^2) \tag{2.4}$$

where q is a concatenated vector with components $q_{x(y)} = p\mathrm{v}_{x(y)}$ (component-wise multiplications), and block (α, β) of matrix C is expressed as follows:

$$C_{j,k,\beta}^{\alpha} = \mathcal{F}^{-1}\left\{ |\mu_k^{\alpha}|^2 \, \mathrm{PSD}_0(f_k^{'}) 2i\pi f_{k,\beta}^{'} \right\}\Big|_{x' = \xi_k d_j - h_k \theta} \tag{2.5}$$

where $\mathcal{F}^{-1}$ denotes inverse Fourier transform, $\xi_k = 1 - h_k / H < 1$ is the cone compression factor for layer k, θ the 2D angular subtense of the LGS WFS pair under consideration, $\beta = x, y$ the spatial frequency directing coupling to wind velocity component β, and μ_k^α a geometrical factor that depends on ξ_k, subaperture size and stencil used to assemble $m_\alpha(x_p, t)$ from the open-loop (or pseudo-open loop) slopes to provide insensitivity to at least tip/tilt (see [16] for details). The zero time delay SLODAR vector is given by

$$b(\tau = 0) = Bp \tag{2.6}$$

where block α of matrix $B \equiv A(\tau = 0)$ is given by (2.5) without the $2i\pi f'_{k,\beta}$ factor in the integrand. In order to factor out τ, we define the following central difference:

$$\delta b(\tau) = \frac{b(\tau) - b(-\tau)}{2\tau} = Cq + \mathcal{O}(\tau^2) \tag{2.7}$$

The $\mathcal{O}(\tau^2)$ term in (2.4) and (2.7) is nonlinear in τ. We have verified that for small lags $\tau < \tau_0$, where τ_0 denotes the atmospheric coherence time, this term is ~2 orders of magnitude smaller than the linear one and can therefore be neglected (it entails a sub-percent level estimation error). The Cn2 profile p and velocity weighted profile q are solved for independently via least-squares fit:

$$\hat{p} = B^{\dagger} b(0), \;\; \hat{q} = (C^T C)^{-1} C^T \delta b(\tau), \tag{2.8}$$

and the wind profile is finally retrieved by component-wise division:

$$\hat{\mathrm{v}}_{x(y)} = \hat{q}_{x(y)} / \hat{p} \tag{2.9}$$

The Cn2 estimator, $B^{\dagger}$, is assembled to guarantee $\hat{p}_k \geq 0$ (see [16] for details). A couple of remarks are in order. (i) The component-wise division in (2.9) is subject to error amplification for weak layers whose strength is at the percent level. Such layers should be masked. It is also desirable to constrain the domain of possible velocity vectors, and mask those falling outside this domain. (ii) The direction of $\hat{\mathrm{v}}_k$ is equal to that of $\hat{q}_k$ since $\hat{\mathrm{v}}_y / \hat{\mathrm{v}}_x = \hat{q}_y / \hat{q}_x$ and is therefore independent of $\hat{p}$.

3. Simulation Results

In this Section, we discuss Monte Carlos simulation results assessing the performance of the above Cn2 and wind profile estimation algorithms when implemented on the TMT LGS MCAO system [3]. This system is equipped with 6 60x60 LGS WFSs with an equivalent subaperture size at the telescope aperture plane equal to $\Delta_{sa} = D / 60 = 0.5$ m, a pentagonal asterism of 70arcsec diameter plus a LGS on-axis, and 2 deformable mirrors (DMs) conjugate to ground level and 12km altitude and driven in closed loop at 800Hz by a tomographic MMSE matrix vector multiply reconstructor using pseudo open loop control [18]. This large (~31K x 7K) control matrix is updated at 0.1Hz using a Fourier Domain Preconditioned Conjugate Gradient (FDPCG) algorithm [10]. Embedded in the control matrix is an intermediate 6-layer tomography step, essential to the meet with margin the 191nm root-mean-square (RMS) WFE requirement averaged over the 17arcsec x 17arcsec science instrument field of view. The following representative integrated turbulence parameters were simulated [19] (all values are quoted at a reference wavelength of 500nm): Fried parameter $r_0 = 17.8$ cm, isoplanatic angle $\theta_0 = 2.8$ arcsec, generalized isoplanatic angle $\theta_2 = 11$ arcsec and Greenwood frequency $f_G = 23$ Hz. Layer altitudes were chosen to match those given by the SLODAR geometry for a 70arcsec wide LGS pair, and wind velocity directions were chosen randomly. The simulated synthetic profile is given in Table 1. All

simulations used a LGS WFS signal level of 750 photo-detected electrons per subaperture per frame, 16x6 pixels per subaperture aligned radially to model a polar coordinate detector with pixels aligned along the elongation direction for the central launch projection geometry [20], and a constrained matched filter processing subaperture pixel intensities into slopes [21].

Table 1 Simulated Cn2 and wind profiles.

Altitude (km)	0	2.85	5.5	8	10.4	12.6
Wind speed (m/s)	5.4	9.7	15.7	20.5	17.1	13.9
Wind direction (deg)	-156	120	45	104	-53	69
Weights (%)	52	26	8	4	4	6

3.1. Known Cn2 and Wind profiles

We start by reviewing the performance of the static MMSE and DKF algorithms without and with perfect wind profile knowledge as reported in [10]. Results are summarized in the top 4 legend entries of Figure 1, and illustrate the non-negligible performance advantage of DKF when the wind velocity profile is perfectly known. The magnitude of this effect is around 35nm RMS in quadrature compared to the MMSE estimator combined with perfect prediction. The bottom 4 legend entries of Figure 1 illustrate that the performance advantage is retained in noise-free simulations, i.e. in the idealized infinite signal-to-noise ratio (SNR) case. This important result suggests that DKF and MMSE have a similar noise gain, but DKF can be tuned to yield superior turbulence rejection than the static MMSE estimator.

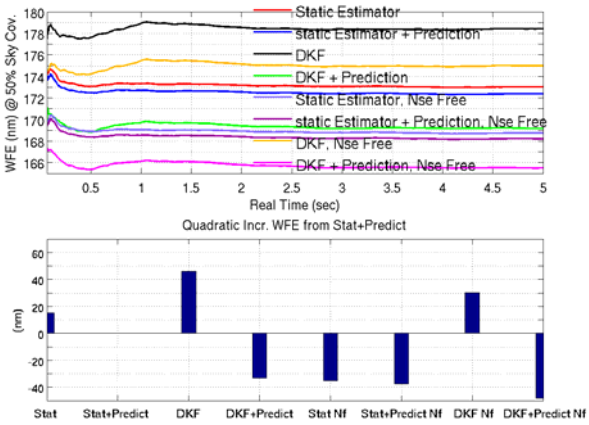

Figure 1 Estimated performance (RMS WFE averaged over 17arcsec x 17arcsec) for static and DKF estimators, without or with perfect prediction for the case of noisy and noise-free WFS pixel intensities.

3.2. Estimated Cn2 and Wind profiles

Next, we study whether the SLODAR algorithm described in Section 2 is accurate enough for DKF to retain its superior turbulence rejection when coupled to it. For this purpose, we accumulated covariance matrix elements (2.1) during 5,200 frames (6.5sec), which corresponds to the number of measurements per LGS WFS and guarantees that the individual measurement covariance and cross-covariance

matrices are full rank. We chose to set the time delay to 1 frame, i.e. $\tau = T_s$, where $T_s = 1/800$ sec. For simplicity, we chose to run the SLODAR algorithm on a single LGS WFS pair, and selected 18 baselines spanning a narrow 1-subaperture wide stripe as shown in Figure 2. Figure 3 illustrates the resulting C matrix defined in (2.5), as well as $C^T C$. Note that both matrices are reasonably well conditioned. The estimated wind profiles (either with known or estimated Cn2 profiles in the denominator of (2.9)) are displayed in Table 2, together with relative estimation errors. The following comments are in order: (i) the Greenwood frequency is accurately estimated around 22.5Hz in both cases, which is a small 2% error from the truth, but (ii) largest wind speed errors are on the order of ~18% on the dominant 3 lowest layers, and increase to ~21% to 34% on top layers when the estimated Cn2 profile is used in (2.9), (iii) largest wind direction errors are on the order of 13%. Figure 4 illustrates that such a level of accuracy brings DKF's performance at the same level as that of the static MMSE estimator combined with perfect prediction, i.e. the 35nm performance gain described in Section 3.1 has unfortunately been lost.

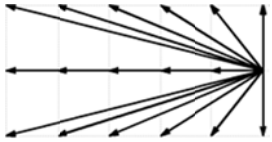

Figure 2 Baseline vector geometry for a single LGS WFS pair.

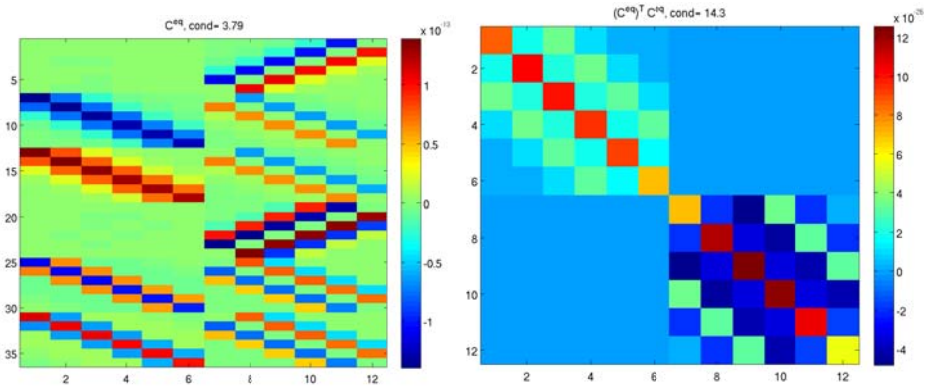

Figure 3: Sample forward matrix C (left) and $C^T C$ (right) for the case of a curvature stencil applied to slopes, i.e. $m_\alpha(x_p) = s_\alpha(x_p - \delta_\alpha) - 2s_\alpha(x_p) + s_\alpha(x_p + \delta_\alpha)$ with $\delta_x = (\Delta_{sa}, 0)$, $\delta_y = (0, \Delta_{sa})$.

Table 2 Estimated wind profiles and relative errors.

Wind speed with known Cn2 (m/s)	4.5	10.2	18.4	17.7	16.3	12.6
Wind speed relative error from truth (%)	17	-5	-17	14	5	9
Wind speed with Cn2 estimate (m/s)	4.7	8.9	18.2	16.2	22.9	11.6
Wind speed relative error from truth (%)	13	8	-16	21	-34	17
Wind direction (deg)	-155	123	51	107	-46	66
Wind direction error from truth (%)	1	-2.5	-13	-3	13	4

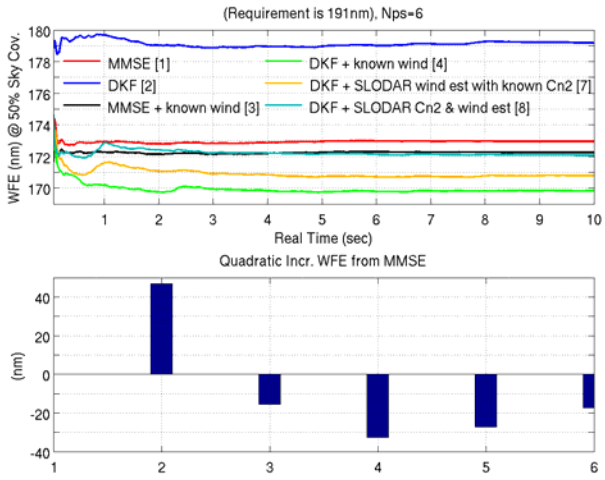

Figure 4 Estimated performance (RMS WFE averaged over 17arcsec x 17arcsec) for static and DKF estimators, without, with perfect or imperfect prediction.

4. Conclusions

We have discussed a SLODAR-based Cn2 and wind profile estimation algorithm and have evaluated its performance when coupled to either a static tomographic MMSE estimator or a tomographic distributed Kalman filter. We found that the superior turbulence rejection of the Kalman filter is a delicate feature requiring wind profile estimation to better than ~20% accuracy. More analysis is needed to understand the limitations of the proposed algorithm as well as its behavior to sense unreconstructed turbulence layers. These questions will be addressed in a forthcoming publication.

5. Acknowledgements

The authors gratefully acknowledge the support of the TMT partner institutions. They are the Association of Canadian Universities for Research in Astronomy (ACURA), the California Institute of Technology and the University of California. This work was supported as well by the Gordon and Betty Moore Foundation, the Canada Foundation for Innovation, the Ontario Ministry of Research and Innovation, the National Research Council of Canada, and the U.S. National Science Foundation. L.Gilles's email address is lgilles@caltech.edu

6. References

1. R.Conan, B.Espeland, M.A.Van Dam and A.H.Bouchez, “Design of the laser tomography adaptive optics system for the Giant Magellan Telescope”, Proc. “Adaptive Optics for Extremely Large Telescopes II” (2012), available online http://ao4elt2.lesia.obspm.fr

2. T.Fusco, S.Meimon, N.Thatte, H.Schnetler, Y.Clenet, M.Cohen, J.Paufique, P.Ammans, F.Clarke, J.L.Dournaux, M.Ferrari, D.Gratadour, N.Hubin, P.Jagourel, V.Michau, C.Petit and M.Tecza, “Laser tomographic AO system for an Integral Field Spectrograph on the E-ELT: the ATLAS project”, Proc. “Adaptive Optics for Extremely Large Telescopes II” (2012), available online http://ao4elt2.lesia.obspm.fr

3. G.Herriot, D.Andersen, J.Atwood, P.Byrnes, C.Boyer, K.Caputa, C.Correia, J.Dunn, B.Ellerbroek, J.Fitzsimmons, L.Gilles, P.Hickson, A.Hill, J.Pazder, V.Reshetov, M.Smith, J.P.Veran, L.Wang and I.Wevers, "NFIRAOS: multi conjugate AO system for TMT", Proc. "Adaptive Optics for Extremely Large Telescopes II" (2012), available online http://ao4elt2.lesia.obspm.fr

4. E.Diolaiti, I.Foppiani, J.M.Conan, C.R.Butler, R.I.Davies, A.Baruffolo, M.Bellazzini, G.Bregoli, P.Ciliegi, G.Cosentino, B.Delabre, T.Fusco, N.Hubin, M.Lombini, E.Marchetti, C.Petit, C.Robert and L.Schreiber, "The E-ELT multi conjugate adaptive optics module", Proc. "Adaptive Optics for Extremely Large Telescopes II" (2012), available online http://ao4elt2.lesia.obspm.fr

5. C.Vogel and Q.Yang, "Fast optimal wavefront reconstruction for multi-conjugate adaptive optics using the Fourier domain preconditioned conjugate gradient algorithm", Opt. Exp. 14, 7487-7498 (2006).

6. L.Gilles and B.Ellerbroek, "Split atmospheric tomography using laser and natural guide stars", J. Opt. Soc. Am. A 25, 2427-2435 (2008).

7. E.Thiébaut and M.Tallon, "Fast minimum variance wavefront reconstruction for extremely large telescopes", J. Opt. Soc. Am. A 27, 1046-1059 (2010).

8. R.Ramlau and M.Rosensteiner, "An efficient solution to the atmospheric turbulence tomography problem using Kaczmarz iteration", Inverse Problems 28, 095004, 1-23 (2012).

9. L.Wang and B.Ellerbroek, "Computer simulations and real-time control of ELT AO systems using graphical processing units", in ``Adaptive Optics Systems III," B.L.Ellerbroek, E.Marcheti and J.P.Véran, eds., Proc. Soc. Photo-Opt. Instrum. Eng. 8447, 844723-1 -844723-11 (2012).

10. L.Gilles, P.Massioni, C.Kulcsar, H.F-Raynaud and B.L.Ellerbroek, "Distributed Kalman filtering compared to Fourier Domain Preconditioned Conjugate Gradient for laser guide star tomography on extremely large telescopes", J. Opt. Soc. Am. A 30, 898-909 (2013).

11. L.Poyneer, M.van Dam and J.P.Véran, "Experimental verification of the frozen flow atmospheric turbulence assumption with use of astronomical adaptive optics telemetry", J. Opt. Soc. Am. A 26, 833-846 (2009).

12. L.Poyneer, B.Macintosh and J.P.Véran, "Fourier transform wavefront control with adaptive prediction of the atmosphere", J. Opt. Soc. Am. A24, 2645-2660 (2007).

13. L.Poyneer and J.P.Véran, "Predictive wavefront control for adaptive optics with arbitrary control loop delays", J. Opt. Soc. Am. A25, 1486-1496 (2008).

14. L.Wang, M.Shoeck and G.Chanan, "Atmospheric turbulence profiling with SLODAR using mutiple adaptive optics wavefront sensors", Appl. Opt. 47, 1880-1892 (2008).

15. A.Cortes, B.Neichel, A.Guesalaga, J.Osborn, F.Rigaut and D.Guzman, "Atmospheric turbulence profiling using multiple laser star wavefront sensors", Mon. Not. R. Astron. Soc. 427, 2089-2099 (2012).

16. L.Gilles and B.L.Ellerbroek, "Real-time turbulence profiling with a pair of laser guide star Shack-Hartmann wavefront sensors for wide-field adaptive optics systems on large to extremely large telescopes", J. Opt. Soc. Am. A **27**, A76-A83 (2010).

17. J.M.Conan, H.F.Raynaud, C.Kucsar, S.Meinon and G.Sivo, “Are integral controllers adapted to the new era of ELT adaptive optics?”, Proc. “Adaptive Optics for Extremely Large Telescopes II” (2012), available online http://ao4elt2.lesia.obspm.fr

18. L.Wang and B.Ellerbroek, “Computer simulations and real-time control of ELT AO systems using graphical processing units”, in ``Adaptive Optics Systems III," B.L.Ellerbroek, E.Marchetti and J.P.Véran, eds., Proc. Soc. Photo-Opt. Instrum. Eng. 844**7**, 844723-1 - 844723-11 (2012).

19. M.Schoeck, S.Els, R.Riddle, W.Skidmore, T.Travouillon, R.Blum, E.Bustos, G.Chanan, S.G.Djorgovski, P.Gillett, B.Gregory, J.Nelson, A.Otarola, J.Seguel, J.Vasquez, A.Walker, D.Walker and L.Wang, “Thirty Meter Telescope Site Testing I: Overview,” Pub. Astron. Soc. Pac. **121**, 384-395 (2009).

20. L.Gilles, L.Wang and B.Ellerbroek, “Impact of laser launch location on the performance of laser tomography and multi conjugate adaptive optics for extremely large telescopes,” Appl. Opt. **49**, G114-G119 (2010).

21. L.Gilles and B.L.Ellerbroek, “Constrained matched filtering for extended dynamic range and improved noise rejection for Shack-Hartmann wavefront sensing”, Opt. Lett. **33**, 1159-1161 (2008).